

This work has been submitted to the IEEE for possible publication. Copyright may be transferred without notice, after which this version may no longer be accessible.

Investigating molecular transport in the human brain from MRI with physics-informed neural networks

Bastian Zapf, Johannes Haubner, Miroslav Kuchta, Geir Ringstad, Per Kristian Eide and Kent-Andre Mardal

Abstract—In recent years, a plethora of methods combining deep neural networks and partial differential equations have been developed. A widely known and popular example are physics-informed neural networks. They solve forward and inverse problems involving partial differential equations in terms of a neural network training problem. We apply physics-informed neural networks as well as the finite element method to estimate the diffusion coefficient governing the long term, i.e. over days, spread of molecules in the human brain from a novel magnetic resonance imaging technique. Synthetic testcases are created to demonstrate that the standard formulation of the physics-informed neural network faces challenges with noisy measurements in our application. Our numerical results demonstrate that the residual of the partial differential equation after training needs to be small in order to obtain accurate recovery of the diffusion coefficient. To achieve this, we apply several strategies such as tuning the weights and the norms used in the loss function as well as residual based adaptive refinement and exchange of residual training points. We find that the diffusion coefficient estimated with PINNs from magnetic resonance images becomes consistent with results from a finite element based approach when the residuum after training becomes small. The observations presented in this work are an important first step towards solving inverse problems on observations from large cohorts of patients in a semi-automated fashion with physics-informed neural networks.

Impact Statement—Physics-informed neural networks have recently demonstrated a significant potential as compared to traditional modeling tools. In this paper we compare a current and popular physics-informed neural network methodology with adjoint based finite element methods for an inverse problem related to a challenging application in brain mechanics. Specifically, we address a contemporary active research area in neuroscience: the so-called glymphatic system which accelerates waste clearance through perivascular spaces. As dementia is commonly associated with accumulation of waste within the brain, a patient-specific assessment of the glymphatic system’s efficiency may be of high clinical value. In this study, we find that physics-informed neural networks are competitive with finite element methods for such application, but the method needs to be set up carefully.

This work was supported in part by the Norwegian Research Council under Grants 300305 and 303362.

Bastian Zapf is with the University of Oslo in Oslo, Norway. (e-mail: bazapf@math.uio.no)

Johannes Haubner and Miroslav Kuchta are with Simula Research Laboratory in Oslo, Norway. (e-mail: haubnerj@simula.no, miroslav@simula.no).

Geir Ringstad is with the Department of Radiology, Oslo University Hospital – Rikshospitalet, Oslo, Norway and the Department of Geriatrics and Internal medicine, Sorlandet Hospital, Arendal, Norway. (e-mail: gringsta@oushf.no)

Per Kristian Eide is with the Institute of Clinical Medicine, Faculty of Medicine, University of Oslo, and the Department of Neurosurgery, Oslo University Hospital – Rikshospitalet in Oslo, Norway. (e-mail: p.k.eide@medisin.uio.no)

Kent-Andre Mardal is with the University of Oslo and Simula Research Laboratory in Oslo (e-mail: kent-and@simula.no).

This paragraph will include the Associate Editor who handled your paper.

Index Terms—Computational biophysics, Inverse problems, Machine learning, Magnetic resonance imaging, Neural networks, Optimal control, Parameter estimation

I. INTRODUCTION

IN the recent years there has been tremendous activity and developments in combining machine learning with physics-based models in the form of partial differential equations (PDE). This activity has lead to the emergence of the discipline “physics-informed machine learning” [1]. Therein, arguably the most popular approach are physics-informed neural networks (PINNs) [2], [3].

PINNs combine PDE and boundary/initial condition into a non-convex optimization problem which can be implemented and solved using mature machine learning frameworks with GPU-acceleration. Furthermore, inverse PDE problems are solved in the same fashion as forward problems in PINNs; the only modification to the code is to add the unknown PDE parameters one seeks to recover to the parameters that the optimizer minimizes over. Among other approaches, e.g., [4], [5], PINNs can be used to discover unknown physics from data. The frequency bias [6] serves as implicit regularization and makes the method less sensitive to noise in inverse settings, making the PINN an appealing approach to addressing inverse PDE problems.

In the context of computational fluid dynamics, PINNs have been successfully applied in inverse problems using simulated data, see, e.g., [7]–[9] and real data [10], [11]. A comprehensive review on PINNs for fluid dynamics can be found in [12]. The successful application of PINNs in these works are a considerable motivation for us to apply them to modeling of the fluid mechanics involved in brain clearance. Various kinds of dementia have recently been linked to a malfunctioning waste-clearance system - the so-called glymphatic system [13]. In this system, peri-vascular flow of cerebrospinal fluid (CSF) plays a crucial role either through bulk flow, dispersion or even as a mediator of pressure gradients through the interstitium [14]. While imaging of molecular transport in either rodents [15] or humans [16] points towards accelerated clearance through the glymphatic system, the detailed mechanisms involved in the system are currently debated [17]–[22].

In this work, we aim to perform a computational investigation of the glymphatic theory based on and similar to [23], [24] with PINNs. Our approach is closely related to [24] where the apparent diffusion coefficient (ADC) for the distribution of gadobutrol tracer molecules over 2 days, as seen in T1-weighted magnetic resonance images (MRI) at certain time

points, is compared with the ADC estimated from diffusion tensor images. The ADC from the T1-weighed images was estimated based on simulations using the finite element method (FEM) for optimal control of the diffusion equation. This approach required careful meshing of the brain geometry and making assumptions on the boundary conditions, but yielded estimates that were robust with respect to regularization parameters. The findings were then compared to estimates of the apparent diffusion coefficient based on diffusion tensor imaging (DTI) [25]. The latter is a magnetic resonance imaging technique that measures the diffusion tensor of water on short time scales, which in turn can then be used to estimate the diffusion tensor for other molecules, such as gadobutrol [24].

A parameter identification problem related to estimating the diffusion coefficient from brain images is solved with high accuracy in [26] with PINNs on simulation data with known boundary conditions. Another work using PINNs related to our problem is [11] where 4D MRI data is used to extract artery pressures. The authors reduce the geometry of the artery to 1-D and hence, taking into account the time dependence of the solution, they effectively solve a two-dimensional problem with PINNs and MRI data. They further use data of considerably high temporal resolution and apply smoothening preprocessing.

The novelty of our work is that we apply PINNs to solve an inverse biomedical flow problem in 4D with unprocessed, noisy and temporally sparse MRI data on a complex domain. We verify the PINN approach on carefully manufactured synthetic data. The synthetic testcases reveal challenges that occur for the PINN due to noise, and we demonstrate how to overcome them by means such as tuning the weights in the PINN loss function. Further, we investigate using the ℓ^1 -norm instead of ℓ^2 -norm for the PDE loss as an alternative to avoid the overfitting. We further discuss how to solve additional challenges that arise when applying the PINN to real MRI data. Throughout the paper, we solve the problem with both PINNs and FEM. We show that, using the proper loss function formulation and training procedure, both methods yield consistent estimates for the apparent diffusion coefficient.

II. PROBLEM STATEMENT

Given a set of concentration measurements $c^d(x_j, t_i)$ at four discrete time points $t_i \in \{0, 7, 24, 46\}$ hours and voxel center coordinates $x_j \in \Omega$, where $\Omega \subset \mathbb{R}^3$ represents a subregion of the brain, we seek to find the optimal diffusion coefficient D such that the discrepancy to the measurement

$$J(c, c^d) = \|c - c^d\|^2 \quad (1)$$

in a suitable norm is minimized under the constraint that $c(x, t)$ fulfills

$$\frac{\partial}{\partial t} c = D \Delta c \quad \text{in } \Omega \times (0, T), \quad (2)$$

where $D > 0$ is the apparent diffusion coefficient. The apparent diffusion coefficient takes into account the tortuosity λ of the extracellular space of the brain and relates to the free diffusion coefficient $D_f = \lambda^2 D$ [27]. Similar to [24] we here made the simplifying assumption of a spatially constant

scalar diffusion coefficient. From the physiological point of view, it is well known that the diffusion tensor in white matter is anisotropic, and hence the modeling assumption of a scalar diffusion coefficient clearly is a simplification. The initial and boundary conditions required for the PDE (2) to have a unique solution are only partially known, and the differing ways in which they are incorporated into the the PINN and FEM approaches are described in sections III-A and III-B.

III. METHODS

A. The PINN approach

In PINNs, the parameter identification problem (1) - (2) can be formulated as an unconstrained non-convex optimization problem over the network parameters θ and the diffusion coefficient D as

$$\min_{\theta, D} \mathcal{J} + w_p \mathcal{L}_p, \quad (3)$$

where $w_p > 0$ is a weighting factor. The data loss \mathcal{J} is defined as

$$\mathcal{J}(c, c^d) = \frac{1}{N_d} \sum_{t_i \in \mathcal{T}} \sum_{x_j \in \Omega} (c(x, t_i) - c^d(x, t_i))^2, \quad (4)$$

where N_d denotes the number of space-time points in $\mathcal{T} \times \Omega$ where we have observations.

The PDE loss term \mathcal{L}_p is defined as

$$\mathcal{L}_p(c, D) = \frac{1}{N_p} \sum_{(x, t) \in \mathcal{P}} |\partial_t c(x, t) - D \Delta c(x, t)|^p, \quad (5)$$

where $p \in [1, \infty)$ and the set \mathcal{P} consists of N_p points in the space-time cylinder $[0, T] \times \Omega_P$ with the PDE domain $\Omega_P \subset \Omega$ defined as the set of coordinates $x \in \mathbb{R}^3$ that lie within *interior* voxels of the domain Ω . The sampling strategy to generate \mathcal{P} is explained in detail in section III-C. In this work we test training with both $p = 2$ and $p = 1$. It is worth noting that boundary conditions are not included (in fact, they are often not required for inverse problems, see, e.g., [2]) in the PINN loss function (3), allowing us to sidestep making additional assumptions on the unknown boundary condition. The initial condition is taken to be the first image at $t = 0$ and simply enters via the data loss term (4).

B. The finite element approach

The parameter identification problem (1) - (2) describes a nonlinear ill-posed inverse problem, cf. e.g. [29]–[31]. We build on the numerical realization of [24] and define the objective function as

$$J(c, c^d) = \sum_{t_i \in \mathcal{T}} \int_{\Omega} (c(x, t_i) - c^d(x, t_i))^2 \, dx. \quad (6)$$

Further, similar to [24], we apply the Tikhonov regularization

$$\begin{aligned} \mathcal{R}((\alpha, \beta, \gamma), g) &= \int_0^T \int_{\partial\Omega} \left(\frac{\alpha}{2} |g|^2 + \frac{\beta}{2} \left| \frac{\partial}{\partial t} g \right|^2 + \frac{\gamma}{2} |\nabla g|^2 \right) \, dS \, dt, \end{aligned} \quad (7)$$

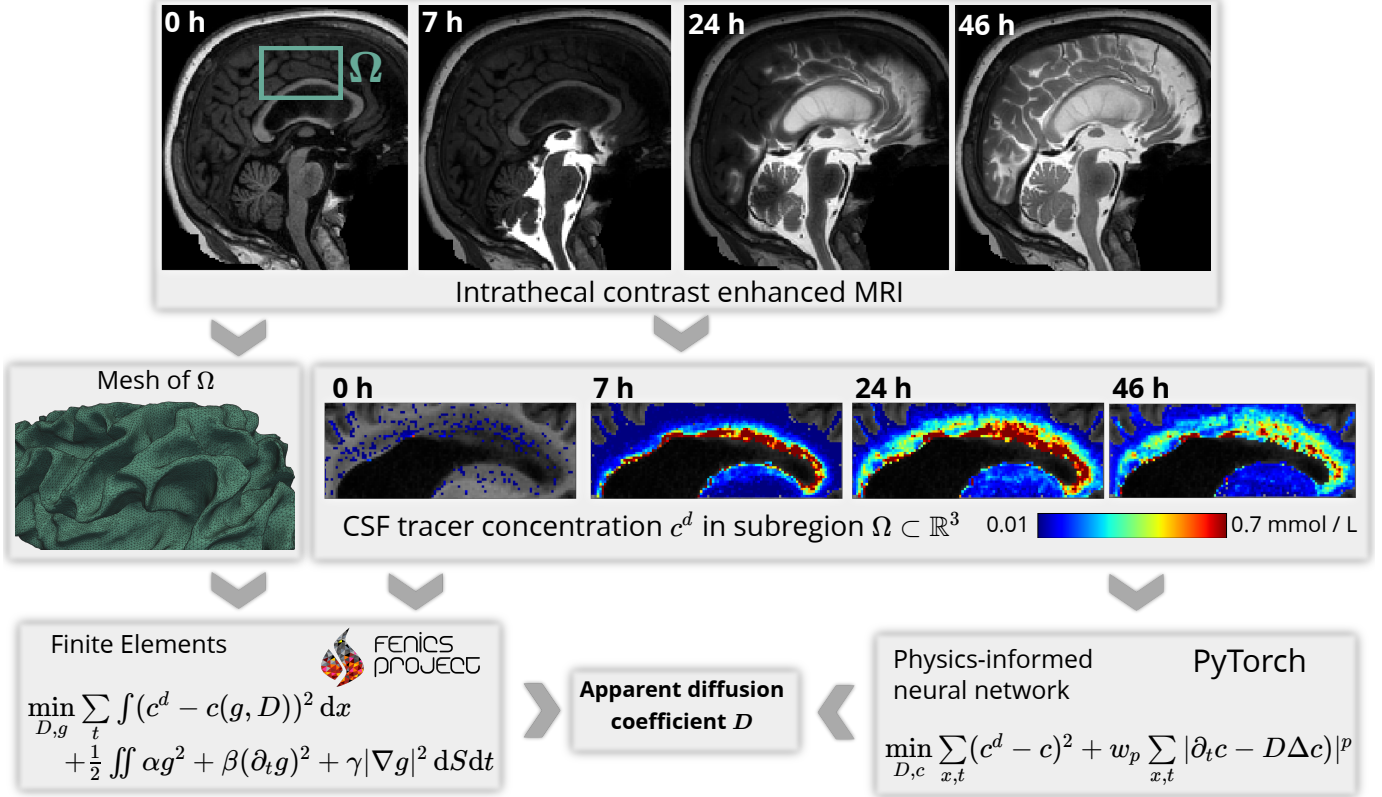


Fig. 1: Flowchart illustrating our workflow from clinical images to estimated tracer diffusivity in the human brain. From the FreeSurfer [28] segmentation of a baseline MRI at $t = 0$, we define and mesh a subregion Ω of the white matter. Intrathecal contrast enhanced MRI at later times $t = 7, 24, 46$ hours are used to estimate the concentration of the tracer in the subregion. We then use both a finite element based approach and physics-informed neural networks to determine the scalar diffusion coefficient that describes best the concentration dynamics in Ω .

for regularization parameters $\alpha, \beta, \gamma > 0$ and formulate the corresponding PDE constrained optimization problem (see e.g. [32]) as

$$\min_{g,D} J(c(g, D), c^d) + \mathcal{R}((\alpha, \beta, \gamma), g), \quad (8)$$

where c solves (2) and satisfies the initial and boundary conditions

$$c(x, t) = g(x, t) \quad \text{on } \partial\Omega \times (0, T), \quad (9)$$

$$c(x, 0) = c_0(x) \quad \text{in } \Omega. \quad (10)$$

Since the realization is based on a reduced formulation using the solution operator of the partial differential equations, the boundary condition $g : \partial\Omega \times (0, T) \rightarrow \mathbb{R}$ needs to be introduced as a control variable.

C. Hyperparameter settings

In the PINN approach, $c : (x, t) \rightarrow \mathbb{R}, x \in \mathbb{R}^3, t \in [0, T]$ is approximated by a feedforward neural network with 9 hidden layers and 64 neurons in each layer and hyperbolic tangent as activation function together with Glorot initialization [33] in all the PINN results presented here. The network furthermore has an input normalization layer with fixed parameters to normalize the inputs to the range $[-1, 1]$. To set these weights, we first compute the smallest bounding box containing all

points $x = (x_1, x_2, x_3) \in \Omega$ to obtain lower and upper bounds $l_i, u_i, i = 1, 2, 3$ such that $l_i \leq x_i \leq u_i$ for $\forall x \in \Omega$. The first layer normalizes the inputs as

$$t \leftrightarrow 2 \frac{t}{T} - 1, \quad x_i \leftrightarrow 2 \frac{x_i - l_i}{u_i - l_i} - 1 \quad (11)$$

for $i = 1, 2, 3$ and with $T = 46$ h (last MRI acquisition timepoint).

If not stated otherwise, we use $N_p = 10^6$ space-time points (x_1, x_2, x_3, t) for the evaluation of the PDE loss (3). We found that this number was either sufficiently high to reach accurate recovery of the diffusion coefficient, or more sophisticated refinement techniques like residual-based adaptive refinement (RAR) [34] were needed instead of simply using more PDE points. The samples for the spatial coordinates x_1, x_2, x_3 are generated by first drawing a random voxel i inside Ω . The voxel center coordinates (x_1^i, x_2^i, x_3^i) are then perturbed to obtain $x_1 = x_1^i + dx$ where x_1^i is the x_1 -coordinate of the center of a randomly drawn voxel i , and similarly for x_2 and x_3 . The perturbation dx is drawn from the uniform distribution $\mathcal{U}([-0.5 \text{ mm}, 0.5 \text{ mm}])$ and ensures that (x_1, x_2, x_3) lies within the voxel i (the voxels correspond to a volume of 1 mm^3). The values for t are chosen from a latin hypercube sampling strategy over the interval $[0, T]$. We furthermore normalize the input data c^d by the maximum value such that $0 \leq c^d \leq 1$. In both the simulation dataset

and the MRI data considered here, we use four images and the same domain Ω . The binary masks describing Ω consists of roughly 0.75×10^4 voxels, i.e., the four images (at 0, 7, 24 and 46 hours) yield a total of $N_d = 3 \times 10^5$ data points. Due to the large number of data and PDE points, we use minibatch sampling of the PINN loss function (3) and minimize it using the ADAM optimizer [35]. The learning rate ν as well as potential learning rate decay schemes are an important hyperparameter, and we specify the used values in each section. The training set is divided into 20 batches, corresponding to 10^4 and 5×10^4 samples per minibatch in the data and PDE loss term, respectively.

Details on the implementation of the minibatch sampling strategy are presented in VI-A. It is worth noting here that our main reason to use minibatch sampling are not memory limitations. The graphics processing units (NVIDIA A100-SXM4) that we use to train the PINN have 80 GB of memory. This is enough to minimize the PINN loss function (3) with $N_d = 3 \times 10^5$ and $N_p = 10^6$ data and PDE loss points in a single batch. Our reason to use minibatch sampling is that the stochasticity of minibatch gradient descent helps to avoid local minima, see, e.g., Chapter 8 in [36]. In Section V-A we perform a systematic study using different minibatch sizes and find that smaller batch sizes are preferable in our setting since they yield more accurate recovery of the diffusion coefficient.

As for the finite element approach, we discretize (2) in time using the Crank-Nicolson scheme and 48 time steps. We then formulate the PDE problem as variational problem and solve it in FEniCS [37] using the finite element method. To limit the compute times required, we use a time step size of 1 h and continuous linear Lagrange elements. We further use linear interpolation of the data as a starting guess for the boundary control g ,

$$g(x, t) = c^d(x, t_i) + \frac{c^d(x, t_{i+1}) - c^d(x, t_i)}{t_{i+1} - t_i} (t - t_i) \quad (12)$$

for $t_i \in \mathcal{T} = \{0, 7, 24, 46\}$ h and $t_i \leq t \leq t_{i+1}$. We then use dolfin-adjoint [38] to compute gradients of the functional (8) with respect to D and g and optimize using the L-BFGS method.

In terms of degrees of freedom (optimization parameters), these settings result in 33665 weights in the neural network. For the finite element approach, the degrees of freedom depend on the number of vertices on the boundary of the mesh since the control is the boundary condition g . Our mesh for Ω has 33398 vertices on the boundary. For 48 time steps, this yields $48 \times 33398 = 1.6 \times 10^6$ degrees of freedom.

D. Parameterization of the diffusion coefficient

Previous findings, e.g. [17], [22], [39], [40] indicate that diffusion contributes at least to some degree to the distribution of tracers in the brain. It can thus be assumed that a vanishing diffusion coefficient is unphysical. This assumption can be incorporated into the model by parameterizing D in terms of a trainable parameter δ as

$$D(\delta) = D_{\min} + \sigma(\delta)D_{\max}, \quad (13)$$

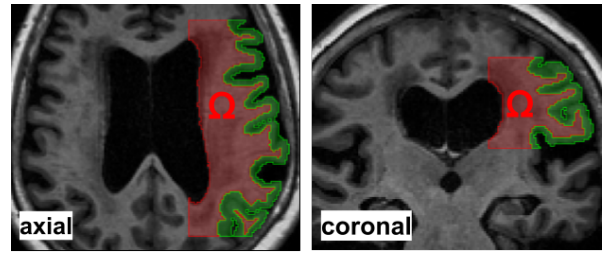


Fig. 2: Axial and coronal slices through the subregion Ω of the white matter we consider in this work. The green region depicts the gray matter and is drawn to illustrate the geometrical complexity of the grey matter.

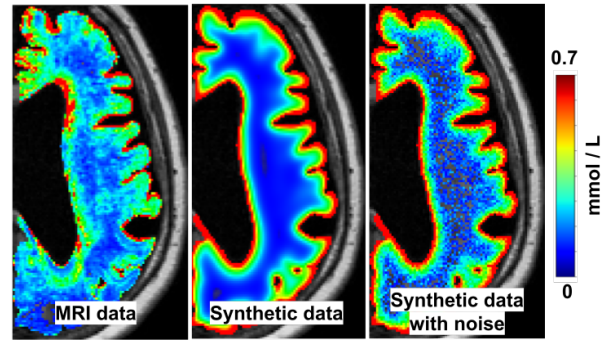


Fig. 3: Axial view of the tracer concentration after 24 h in the right hemisphere for the three data sets considered in this work. In the MRI data it can be seen how the tracer enters the brain from CSF spaces (black). This observation motivates the boundary condition (15) that is used to generate the synthetic data via simulations.

where $\sigma(x) = (1 + \exp(-x))^{-1}$ denotes the logistic sigmoid function. In all results reported here, we initialize with $\delta = 0$ and set $D_{\min} = 0.1 \text{ mm}^2 \text{ h}^{-1}$ and $D_{\max} = 1.2 \text{ mm}^2 \text{ h}^{-1}$. This parametrization with a sigmoid function effectively leads to vanishing gradients $|\frac{\partial D}{\partial \delta}|$ for $|\delta| \gg 1$. In section V-B we demonstrate that this can help to avoid instabilities that occur during PINN training without parameterization, i.e.

$$D = \delta. \quad (14)$$

The reason to introduce a $D_{\min} > 0$ is to avoid convergence into a bad local minimum. For the finite element approach, we did not observe convergence into a local minimum where $D = 0$, and hence used the parameterization (14) as in [24].

IV. DATA GENERATION

A. MRI Data

The data under consideration in this study is based on MRI scans taken of a patient who was imaged at Oslo University Hospital in Oslo, Norway. The patient was diagnosed with normal pressure hydrocephalus and is referred to as "NPH1" in [24].

The imaging protocol starts with the acquisition of a baseline MRI before 0.5 mL of a contrast agent (1 mmol/mL gadobutrol) is injected into the CSF at the spinal canal (intrathecal injection). The pulsating movement of CSF transports

the tracer towards the head where it enters the brain. The contrast agent alters the magnetic properties of tissue and fluid, and in subsequently taken MRI, enriched brain regions display changes in MR signal relative to the baseline MRI. From the change in signal we estimate the concentration of tracer per voxel at timepoints 0, 7, 24 and 46 hours after injection. Further details on the MRI acquisition and tracer concentration estimation can be found in [24].

We next use FreeSurfer [28] to segment the baseline image into anatomical regions and obtain binary masks for white and gray matter. The human brain has many folds and represents a highly complex geometry. To limit the intrinsically high computational requirements of inverse problems, we focus on a subregion of the white matter shown in Fig. 2.

In the following, we describe how this data is processed further to obtain patient-specific finite element meshes to generate synthetic test data by simulation.

B. Synthetic data

We use the surface meshes created during the brain segmentation with FreeSurfer [28] to create finite element meshes of Ω . The surface are loaded into SVMTK [41], a Python library based on CGAL [42], for semi-automated removal of defects and creation of high quality finite element meshes. Details on SVMTK and the mesh generation procedure can be found in [43]. Using FEM we then solve the boundary value problem given by (2) and (9), (10) with a diffusion coefficient $D_0 = 0.36 \text{ mm}^2 \text{ h}^{-1}$. This value for the diffusion of Gadobutrol was estimated in [24] from diffusion tensor imaging (DTI). In detail, we discretize (2) using the Crank-Nicolson scheme and use integration by parts to transform (2) into a variational problem that is solved in FEniCS [37] with linear Lagrange elements. We use a high mesh resolution mesh with 3×10^5 vertices (10^6 cells) and small time step of 16 min. In combination with the Crank-Nicolson scheme, this minimizes effects of numerical diffusion. For the initial condition (10) we assume no tracer inside the brain at $t = 0$, i.e. $c_0 = 0$. The boundary condition (9) is assumed to be spatially homogeneous while we let the datum g vary in time as

$$g(t) = \begin{cases} 2t/T & \text{for } 0 \leq t \leq T/2 \\ 2 - 2t/T & \text{for } T/2 \leq t \leq T. \end{cases} \quad (15)$$

This choice leads to enrichment of tissue similar to what is observed experimentally over the timespan of $T = 46$ hours. Finally, we interpolate the finite element solution $c(x, t)$ between mesh vertices and evaluate it at the center coordinates x_{ijk} of the voxels ijk inside the region of interest Ω and store the resulting concentration arrays c_{ijk} at 0, 7, 24 and 46 hours. With this downsampling procedure, we are then able to test the methods within the same temporal and spatial resolution as available from MRI.

C. Synthetic data with artificial noise

We test the susceptibility of the methods with respect to noise by adding to the data perturbations drawn randomly from the normal distribution $\mathcal{N}(0, \sigma^2)$. We refer to the standard

deviation σ as noise level hereafter. Since negative values for the concentration c are nonphysical, we threshold negative values to 0, i.e. the noise-corrupted voxel values are computed as

$$c_{ijk} = \max\{0, c_{ijk} + \eta\} \quad \text{where } \eta \sim \mathcal{N}(0, \sigma^2). \quad (16)$$

In all the results presented in this work, we choose $\sigma = 0.05$. This corresponds to 5 % of the maximum value in the simulated measurements c_{ijk} and allows to reproduce some of the characteristic difficulties occurring when applying the PINN to the clinical data considered here.

V. RESULTS

A. Synthetic data

We first verify the implementation of the two approaches by considering synthetic data without noise, cf. Fig. 3, in the white matter subregion Ω depicted in Fig. 2.

For the PINN we test different minibatch sizes for three different optimization schemes using the ADAM optimizer: (i) fixed learning rate 10^{-3} and $p = 2$, (ii) fixed learning rate 10^{-3} while we switch from $p = 2$ to $p = 1$ after half the epochs and (iii) using initial learning rate 10^{-3} that decays exponentially during training to 10^{-4} and $p = 2$. Table IV in the appendix tabulates the relative error between the learned diffusion coefficient and the ground truth D_0 for a wide range of parameters. We find that (a) in general smaller batch sizes result in more accurate results and (b) the results are both most stable and accurate when using exponentially decaying learning rate. Notably, the PINN recovers the ground truth diffusion coefficient D_0 to up to 1 % accuracy when using the learning rate decay optimization scheme. These result are in line with [44] where increased accuracy in parameter recovery was observed for smaller batch sizes. There are also settings where full batch optimization with L-BFGS improves PINN performance in parameter identification problems [45].

For the finite element approach, table V in the appendix presents the accuracy of the recovered diffusion coefficient. According to the theoretical results, decreasing regularization parameters leads to higher accuracy but less well conditioned optimization problems. This is in line with the results presented in table V. The finite element approach with appropriate regularization parameters and the PINN approach yield comparably accurate results.

B. Synthetic data with noise

We next discuss how to address challenges that arise for the PINN when trained on noisy data as specified by (16). From Table IV we found that smaller batch sizes of $\sim 10^4$ points per loss term result in more accurate recovery of the diffusion coefficient (for fixed number of epochs). We hence divided data and PDE points into 20 batches with 1.5×10^4 and 5×10^4 samples per batch, respectively, for the following results.

In Fig. 4 it can be observed that the recovered diffusion coefficient converges to the lower bound $D_{\min} = 0.1 \text{ mm}^2 \text{ h}^{-1}$ during training with ADAM and exponential learning rate decay from 10^{-3} to 10^{-4} . This effect is due to overfitting to

the data and can be prevented by increasing the regularizing effect of the PDE loss via increasing the PDE weight w_p . We observe from Fig. 4 that for $w_p \gtrsim 64$ the recovered D converges towards the true value to within $\approx 10\%$ error. It can also be seen that increasing the weight further does not significantly increase the accuracy. Fig. 5 (b) and (c) shows the predicted solution after 46 h of the trained PINN. It can be seen that the overfitting occurring for $w_p = 1$ is prevented by choosing a higher weight such as $w_p = 64$.

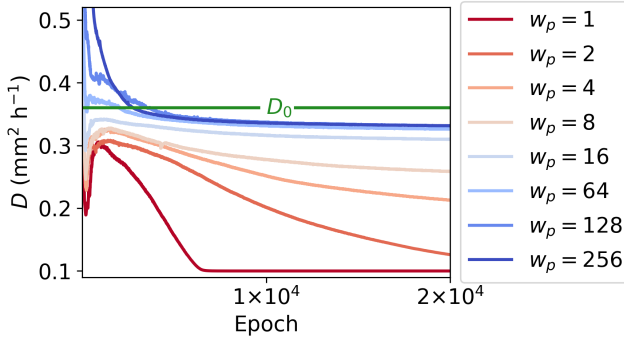


Fig. 4: The diffusion coefficient recovered by the PINN trained on noisy simulation data converges to D_{\min} for PDE weight $w_p \leq 2$ in the loss function (3). As demonstrated in Fig. 5, this is due to overfitting of noise.

These results are in line with the frequent observation that the weights of the different loss terms in PINNs are critical hyperparameters. Several works have put forth methodologies to choose these weights adaptively during training [46]–[48], but in practice these weights are often chosen via trial-and-error. Furthermore, in settings with noisy data, it can not be expected that both data loss and PDE loss become zero. The ratio between PDE weight and data weight reflects to some degree the amount of trust one has into the data and the physical modeling assumptions, i.e., the PDE. In other words, adaptive strategies that are based on the interpretation of the different terms in the PINN loss as a multiobjective minimization problem, are impractical in our setting. Since we assume that the data is governed by a diffusion equation (with unknown diffusion coefficient), we want the PDE residual to become small. As demonstrated above, this can be achieved by increasing the PDE weight. The correlation between a large weight and the low PDE residual and the more accurate recovery of the diffusion coefficient is visualized in Fig. 6.

Fig. 6 also demonstrates the effectiveness of another strategy to successfully lower the PDE residual, which is based on using the ℓ^1 -norm for the PDE loss. Exemplarily, we demonstrate the effectiveness of this approach in Fig. 5 (d). There, we plot the PINN prediction after training with $p = 1$. It can be seen that the prediction is visually identical to the prediction obtained with $p = 2$ and $w_p = 64$ (The relative difference between the predictions in Fig. 5 (c) and (d) is about 2 %).

The results in Fig. 6 are obtained in a systematic study with fixed $w_p = 1$. In detail, we test the combinations of the following hyperparameters:

- Parameterizations $D(\delta)$ (13) vs $D = \delta$ (14)

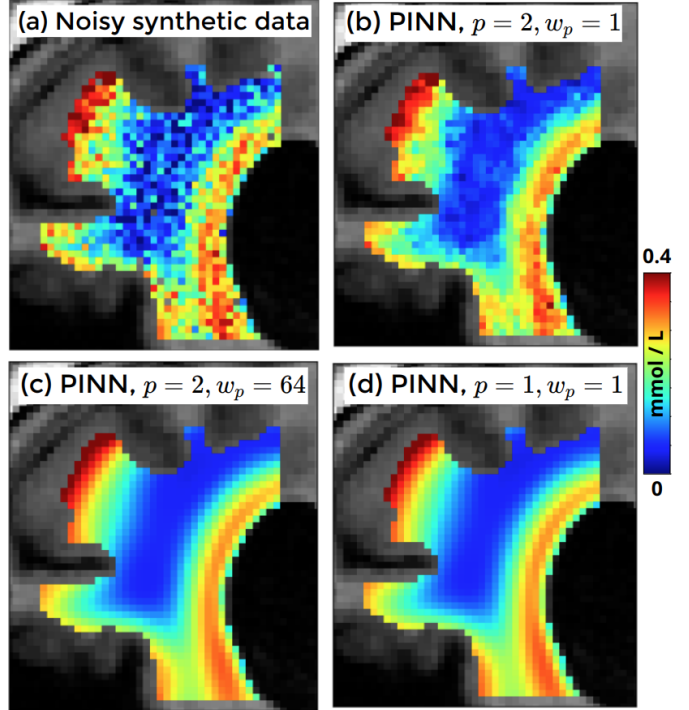


Fig. 5: Coronal slice of synthetic data with noise after 46 h (a), compared to prediction of PINN after training with different hyperparameters in the loss function (3). The overfitting seen in the PINN with $p = 2, w_p = 1$ (b) can be prevented by using either increased PDE weight w_p (c) or the ℓ^1 -norm for the PDE loss (d).

- $p = 1$, switching $p = 2 \rightarrow 1$ after half the epochs, $p = 2$
- fixed learning rate 10^{-3} , exponential learning rate decay $10^{-3} \rightarrow 10^{-4}$, fixed learning rate 10^{-4} and exponential learning rate decay $10^{-4} \rightarrow 10^{-5}$,

Table I reports the relative error in the recovered diffusion coefficient after 2×10^4 epochs of training with ADAM and the minibatch algorithm 1. From the Table it can be observed that for $D = \delta$ and $p = 1$ instabilities occur with the default learning rate 10^{-3} and, due to exploding gradients, the algorithm fails. This problem does not occur when using the parameterization $D = D(\delta)$ (13). It can further be observed that both parameterizations can be fine tuned to achieve accuracy $\lesssim 10\%$. However, the table shows that it is *a priori* not possible to assess which hyperparameter setting performs best.

We hence investigate the effect of the different hyperparameters on the trained PINN and compute the ℓ^1 -norm of the residual after training defined as

$$\frac{1}{|\Omega_P|} \sum_{t \in \tau} \sum_{x \in \Omega_P} |\partial_t c(x, t) - D \Delta c(x, t)|. \quad (17)$$

Here, $\tau = \{0, \dots, T\}$ are 200 linearly spaced time points between first and final image at $T = 46$ h and Ω_P denotes the set of center coordinates of all the voxels inside the PDE domain. Note that we evaluate (17) with the recovered diffusion coefficient, not with the true D_0 . Table II reports this norm for the different hyperparameter settings. It can be

seen that different hyperparameters lead to different norms of the PDE residual. Comparing Tables I and II reveals that low values of the residual correspond to more accurate recovery of the diffusion coefficient. These results are plotted together with the results from Fig. 4 in Fig. 6. This underlines our observation that it is important in our setting to train the PINN such that the norm of the PDE residual is small.

TABLE I: Rel. error $|D - D_0|/D_0$ in % in the diffusion coefficient for different optimization strategies averaged over 4 trainings on synthetic data with noise. Comparing to Table II reveals that the accuracy correlates with the PDE residual after training, i.e. the lower the PDE residual, the more accurate the recovered diffusion coefficient. This relation is further illustrated in Fig. 6. Failure of the algorithm is indicated by the symbol "x".

Parameterization	lr	10^{-3}	$10^{-3} \rightarrow 10^{-4}$	10^{-4}	$10^{-4} \rightarrow 10^{-5}$
	p				
$D = \delta$	1	x	x	18	43
	$2 \rightarrow 1$	x	7	3	13
	2	70	83	16	17
$D = D(\delta)$	1	7	2	24	39
	$2 \rightarrow 1$	11	11	9	18
	2	72	72	13	19

TABLE II: Norm of the residual after training for different optimization strategies. Comparing to Table I reveals that low values of the PDE residual correspond to accurate recovery of D . Failure of the algorithm is indicated by the symbol "x".

Parameterization	lr	10^{-3}	$10^{-3} \rightarrow 10^{-4}$	10^{-4}	$10^{-4} \rightarrow 10^{-5}$
	p				
$D = \delta$	1	x	x	1.6e-02	3.4e-02
	$2 \rightarrow 1$	x	9.7e-03	1.4e-02	3.4e-02
	2	1.5e+00	6.1e-01	2.4e-01	3.0e-01
$D = D(\delta)$	1	1.1e-02	5.7e-03	2.1e-02	3.9e-02
	$2 \rightarrow 1$	2.1e-02	1.0e-02	2.9e-02	6.1e-02
	2	7.3e-01	7.7e-01	2.7e-01	4.7e-01

Table III tabulates the relative error in the recovered diffusion coefficient for solving (8)–(10) with regularization parameters spanning several orders of magnitude. The results are in line with the well-established observation that a sophisticated decrease of the noise level and regularization parameters ensures convergence towards a solution, see, e.g., [49, Sec. 1.1].

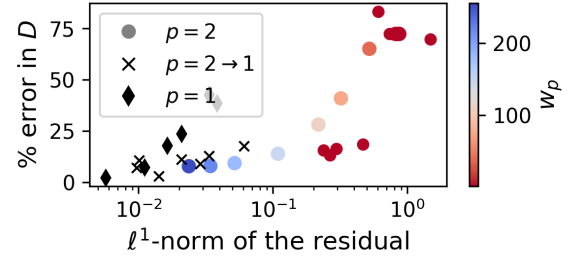


Fig. 6: Relative error in recovered D from noisy synthetic data as a function of the residual after training for the results presented in Fig. 4 and Tables I-II. Color encodes the PDE weight $1 \leq w_p \leq 256$ for the results with $p = 2$ (dotted). Different hyperparameter settings in the PINN loss (3) yield models which fulfill the PDE to different accuracy, and low values for the residual coincide with more accurate recovery of the diffusion coefficient.

TABLE III: Rel. error $|D - D_0|/D_0$ in % for the finite element approach (8), different regularization parameters. Failure of the algorithm is indicated by the symbol "x". Convergence plots for the optimization are given in Fig. 14.

α	β	γ	0.0	0.01
10^{-6}	0.0		43	10
	0.01		8	x
	0.1		4	x
10^{-4}	0.0		44	x
	0.01		5	13
	0.1		6	12

C. MRI Data

We proceed to estimate the apparent diffusion coefficient governing the spread of tracer as seen in MRI images. It is worth emphasizing here that our modeling assumption of tracer transport via diffusion with a constant diffusion coefficient $D \in \mathbb{R}$ is a simplification, and that we can not expect perfect agreement between model predictions and the MRI data. Furthermore, closer inspection of the tracer distribution on the boundary in Fig. 3 reveals that, unlike in the synthetic data, the concentration varies along the boundary in the MRI measurements. Based on these two considerations it is to be expected that challenges with the PINN approach arise that were not present in the previous, synthetic testcases. However, our previous observation that smaller PDE residual correlates with more accurate recovery of the diffusion coefficient serves as a guiding principle on how to formulate and minimize the PINN loss function such that the PDE residual becomes small.

Based on the observation that the parameterization $D = D(\delta)$ avoids instabilities during the optimization, we only use this setting in this subsection. The white matter domain Ω is the same as in the previous section, and we again divide both data and PDE loss into 20 minibatches. We train for 10^5 epochs using the ADAM optimizer with exponentially decaying learning rate 10^{-4} to 10^{-5} .

For $p = 2$ we test with PDE weight

$$w_p \in \{1, 32, 64, 128, 256, 512, 1024\} \quad (18)$$

and display the results in Fig. 7.

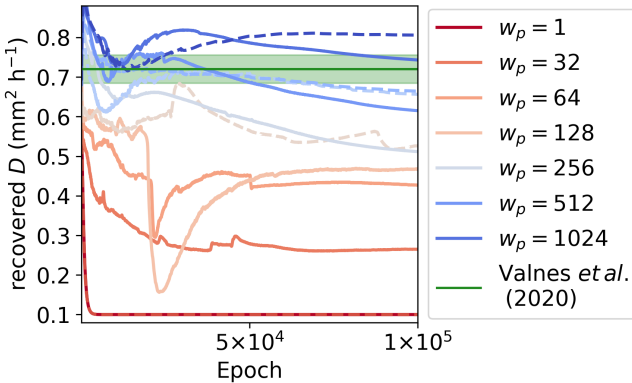


Fig. 7: Diffusion coefficient during training for different PDE weights w_p and exponentially decaying learning rate from 10^{-4} to 10^{-5} . Dashed lines indicate result with RAR. Shaded green stripe represents the error estimate for D from Valnes *et al.* [24].

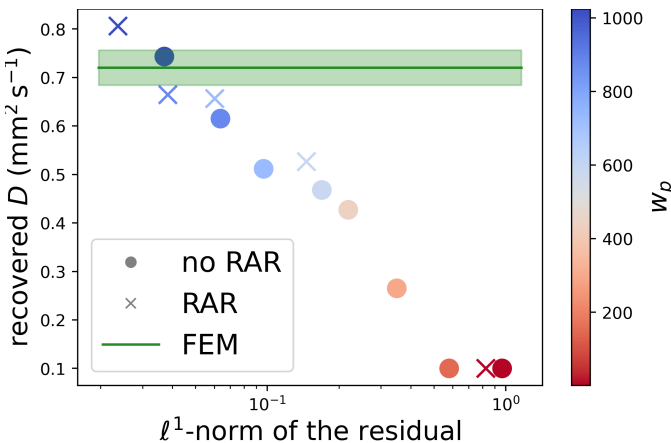


Fig. 8: Estimated diffusion coefficient with $p = 2$ for different PDE weights w_p as a function of the ℓ^1 -norm of the residual after training. The values for FEM is taken from Valnes *et al.* [24], the shaded horizontal bars indicates the error estimate from [24].

In Fig. 9 we plot the ℓ^1 -norm of the residual as a function of time $t \in [0, T]$, defined as

$$r(t) = \frac{1}{|\Omega_P|} \sum_{x \in \Omega_P} |\partial_t c(x, t) - D \Delta c(x, t)|. \quad (19)$$

The continuous blue lines in Fig. 9 exemplarily show $r(t)$ for some PDE weights. It can be seen that higher PDE weights lead to lower residuals. However, for $w_p = 256$ the PDE residual is significantly higher at the times where data is available and in between. We did not observe this behavior in the synthetic testcase. Since we want the modeling assumption (2) to be fulfilled equally in $\Omega \times [0, T]$, we use residual based adaptive refinement (RAR) [34]. Using the RAR algorithm, we add 10^5 space-time points to the set \mathcal{P} of PDE points after $1 \times 10^4, 2 \times 10^4, \dots, 9 \times 10^4$ epochs. Details on our

implementation of RAR are given in Appendix VI-C. The effectiveness of RAR to reduce this overfitting is indicated by the dashed blue lines in Fig. 9.

For $p = 1$ we test with an exponentially decaying learning rate from 10^{-3} to 10^{-4} as well as 10^{-4} to 10^{-5} . With this setting, the PINN finds an estimate $D = 0.75 \text{ mm}^2 \text{ h}^{-1}$ which is close to [24] who found $D = 0.72 \text{ mm}^2 \text{ h}^{-1}$. However, a closer inspecting of the PINN prediction at 22, 24 (where data is available) and 26 hours shown in Fig. 12 reveals that the PINN is overfitting the data. This is further illustrated by the continuous red line in Fig. 9 where it can be seen that the PDE residual is one order of magnitude higher at the times where data is available. The dashed red line in Fig. 9 and the right panel in Fig. 12 show that this behavior can be prevented by using RAR.

Since the RAR algorithm increases the number of PDE points, the compute time increases (by about 25 % in our setting). We hence test a modification of the RAR algorithm. Instead of only adding points, we also remove the points from \mathcal{P} where the PDE residual already is low. We here call this procedure residual based adaptive exchange (RAE) and give the details in Appendix VI-C. The dotted red line in Fig. 9 demonstrates that in our setting both methods yield similarly low residuals $r(t)$ without overfitting the data. Since in RAE the number of PDE points stays the same during training, the compute time is the same as without RAR. In Fig. 10 it can be seen how both RAR and RAE add more PDE points around the timepoints where data is available.

We estimate the apparent diffusion coefficient D by averaging over 5 trainings with either RAR or RAE and learning rate decay from 10^{-3} to 10^{-4} or 10^{-4} to 10^{-5} . The results are displayed in Fig. 11 together with the ℓ^1 -norm (17) after training. It can be seen that for the same learning rate, both RAR and RAE yield similar results. A lower learning rate, however, leads to lower PDE residual and an estimated diffusion coefficient which is closer to the value $0.72 \text{ mm}^2 \text{ h}^{-1}$ from [24].

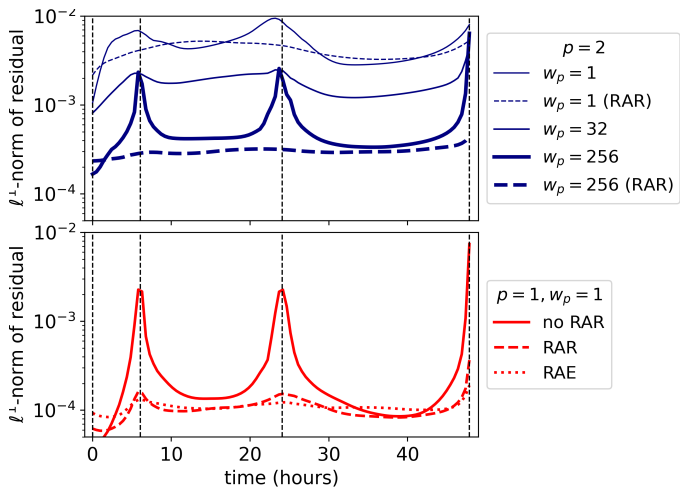


Fig. 9: Average PDE residual in Ω_P over time for different optimization schemes. Vertical lines (dashed) indicate the times where data is available. In all cases, the learning rate decays exponentially from 10^{-3} to 10^{-4} .

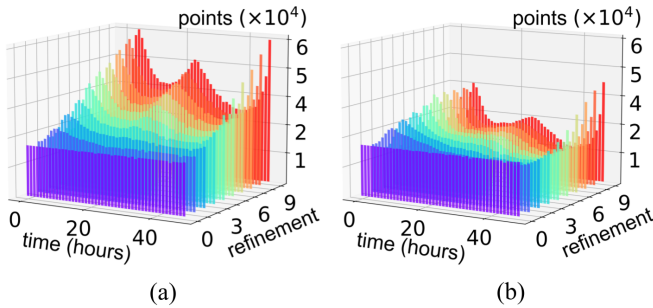


Fig. 10: Distribution of PDE points during training with RAR (a) and RAE (b). Starting from a uniform distribution of points (in time), the algorithms add more points at 7, 24 and 46 hours where data is available.

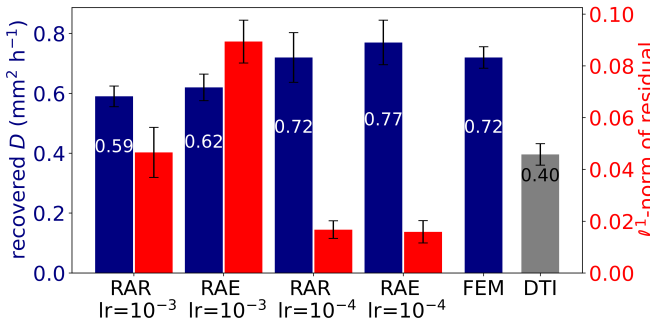


Fig. 11: Blue: PINN estimates for the diffusion coefficient with RAR or RAE and different initial learning rates ($p = 1$ in all cases). Red: ℓ^1 -norm of the residual after training. It can be seen that lower learning rate leads to a lower residual norm and an estimate for the diffusion coefficient closer to the FEM approach [24].

D. Testing different patients

In [24], the same methodology was applied to two more patients, named 'REF' and 'NPH2'. We use a similar subregion of the white matter as in [24] but remove the voxels on the boundary of the domain. The PINN is used with the following hyperparameters from section V-C that yielded the lowest PDE residual after training: The number of minibatches is set to 20, training for 10^5 epochs with ADAM and exponential learning rate decay from 10^{-4} to 10^{-5} , and $p = 1$ with RAR at $1 \times 10^4, 2 \times 10^4, \dots, 9 \times 10^4$ epochs. The network architecture remains the same. We find $D = 0.41 \text{ mm}^2 \text{h}^{-1}$ for patient 'REF' while [24] found $D = 0.50 \text{ mm}^2 \text{h}^{-1}$. For patient 'NPH2' we find $D = 0.48 \text{ mm}^2 \text{h}^{-1}$ while [24] found $D = 0.50 \text{ mm}^2 \text{h}^{-1}$.

VI. DISCUSSION

In this work, we have tested both physics informed networks and adjoint based finite element methods for assessing the apparent diffusion coefficient in a geometrically complex domain, a subregion of the white matter of the human brain, based on a few snapshots of T1-weighted contrast enhanced MR images over the course of 2 days. Both methodologies

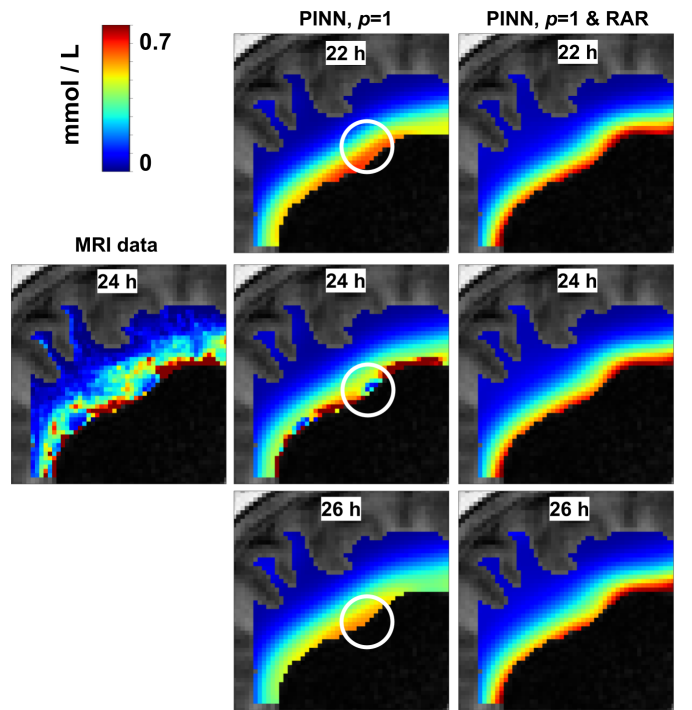


Fig. 12: Upper row: Zoom into a sagittal slice of PINN prediction at 22 hours with $p = 1$ and $p = 1$ & RAR after training. Middle row: Zoom into a sagittal slice of data at 24 h, and PINN prediction prediction at 24 hours. Lower row: Prediction of the PINNs two hours after the data snapshot. Comparing the concentration in the white circle indicates that the PINN trained with $p = 1$ overfits the data.

yield similar estimates when properly set up, that is; we find that the ADC is in the range $(0.6\text{--}0.7) \text{ mm}^2 \text{h}^{-1}$, depending on the method, whereas the DTI estimate is $0.4 \text{ mm}^2 \text{h}^{-1}$. As such the conclusion is similar to that of [24].

From the mathematical point of view, we have sought the solution of a challenging nonlinear ill-posed inverse problem with limited and noisy data in both space and time. There can thus be more than one local minimum and the accuracy of the estimated solutions depends on the regularization and/or hyper parameters. Moreover, the limited amount of available data prevents from quantifying the uncertainty in the recovered parameters, but such modeling studies represent a first step towards methodology that may have great clinical implications.

In general, we believe that the current problem serves as a challenging test case and is well suited for comparing PINNs and FEM based methods. Further, since the finite element approach is well-established and theoretically founded it can serve to benchmark PINNs. Our numerical results indicate that the norm of the PDE residual of the trained PINN correlates with the quality of the recovered parameter. This relates back to the finite element approach where the PDE residual is small since the PDE is explicitly solved. For the PINNs, we have found that in particular two methodological choices help to significantly lower the PDE: ℓ^1 -penalization of the PDE and adaptive refinement of residual points. Given this setup, PINNs are as accurate as FEM and, given, the existent implementation

levering GPU acceleration, they are potentially more efficient than FEM.

From the physiological point of view, there are several ways to improve upon our modeling assumption of a spatially constant, scalar diffusion coefficient. For instance, as proposed by [40] an estimate of the local CSF velocity can be obtained by the optimal mass transport technique. From an implementational point of view, such methods fit well within our current framework since the PINN formulation is comparably easy to implement and the PDE does not have to be solved explicitly.

Our main observation is that the apparent diffusion coefficient recovered by PINNs approaches the FEM result for decreasing values of the PDE residual after training. We consider it a strong result that we are able to obtain so similar results with such vastly different methods as neural networks and finite elements.

APPENDIX

A. Minibatch sampling for PINNs

Algorithm 1 Minibatch training

Input: neural network Φ with parameters θ , data minibatch size n_d , PDE minibatch size n_r , RAR_checkpoints $\{i_1, \dots, i_n\}$, epochs, learning rate η , initial guess D for the diffusion coefficient, input-data pairs $\{(\mathbf{x}_d^k, c_d^k) \in \mathbb{R}^4 \times \mathbb{R}\}_{1 \leq k \leq N_d}$, collocation points $\{\mathbf{x}_r \in \mathbb{R}^4\}_{1 \leq k \leq N_r}$

- 1: compute number of data batches $b_d = \text{ceil}(N_d/n_d)$
- 2: compute number of PDE batches $b_r = \text{ceil}(N_r/n_r)$
- 3: Set $b = \max(b_d, b_r)$
- 4: **for** i in range(epochs) **do**
- 5: **if** $i \in \text{RAR_checkpoints}$ **then**
- 6: refine collocation points with either Algorithm 2 or 3
- 7: **end if**
- 8: randomly split $\{(\mathbf{x}_d^k, c_d^k)\}$ into subsets $\mathcal{D}_{1 \leq j \leq b_d}$
- 9: randomly split $\{\mathbf{x}_r^k\}$ into subsets $\mathcal{R}_{1 \leq j \leq b_r}$
- 10: # Iterate over all minibatches
- 11: **for** j in range(b) **do**
- 12: # Start from beginning should you reach the last subset in \mathcal{D}_{b_k} or \mathcal{R}_{b_r} , respectively (Happens if $b_r \neq b_d$):
- 13: Set $j_d = j \bmod b_d$, $j_r = j \bmod b_r$
- 14: # Compute losses on subsets
- 15: $\mathcal{L} = \frac{1}{|\mathcal{R}_{j_d}|} \sum_{\mathbf{x}, c \in \mathcal{D}_{j_d}} (\Phi(\mathbf{x}) - c)^2$
- 16: $\mathcal{L} += \frac{1}{|\mathcal{R}_{j_r}|} \sum_{\mathbf{x} \in \mathcal{R}_{j_r}} |\partial_t \Phi(\mathbf{x}) - D \Delta \Phi(\mathbf{x})|^p$
- 17: # update parameters θ
- 18: $\theta = \eta \nabla_{\theta} \mathcal{L}$
- 19: # update diffusion coefficient D
- 20: $D = \eta \nabla_D \mathcal{L}$
- 21: **end for**
- 22: **end for**

TABLE IV

Average rel. error $|D_{\text{pinn}} - D_0|/D_0$ in % after 2×10^4 epochs training on synthetic data without noise, with Algorithm 1. We average over 5 runs, numbers in brackets are standard deviation.

Optimization scheme	$n_d \backslash n_r$	10 ⁴	5 \times 10 ⁴	10 ⁵
		10 ⁴	5 \times 10 ⁴	10 ⁵
ADAM lr = 1e-3 $p = 2$	10000	2 (0)	2 (1)	3 (1)
	33334	4 (0)	12 (6)	9 (1)
	50000	7 (1)	5 (0)	2 (0)
	100000	7 (1)	55 (18)	59 (18)
	166667	8 (1)	24 (17)	50 (23)
	333334	8 (1)	38 (4)	50 (16)
ADAM lr = 1e-3 $p=2 \rightarrow p=1$	10000	2 (0)	1 (0)	2 (0)
	33334	2 (0)	2 (0)	2 (0)
	50000	2 (1)	2 (0)	2 (1)
	100000	2 (1)	58 (27)	50 (25)
	166667	2 (1)	3 (2)	68 (4)
	333334	2 (0)	0 (0)	62 (6)
ADAM exp lr decay $1e-3 \rightarrow 1e-4$ $p = 2$	10000	1 (0)	1 (0)	1 (0)
	33334	1 (0)	1 (1)	1 (0)
	50000	1 (1)	1 (0)	1 (0)
	100000	1 (0)	10 (6)	72 (0)
	166667	1 (1)	4 (2)	23 (26)
	333334	1 (0)	4 (4)	59 (23)

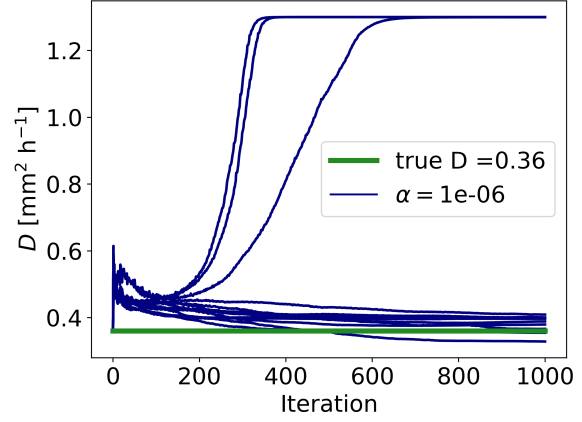


Fig. 13: Convergence plots for the FEM regularization parameters presented in table V.

B. Finite element solution of the synthetic testcase

TABLE V: Rel. error $|D - D_0|/D_0$ for the FEM approach (8), different regularization parameters, 3 measurement points, clean data, 1,000 iterations. Convergence of the optimization is demonstrated in Fig. 13

α	$\beta \backslash \gamma$	0.0	0.01	1.0	
		0.001	9	8	261
10^{-6}	0.01	1	5	261	
	0.1	11	10	261	

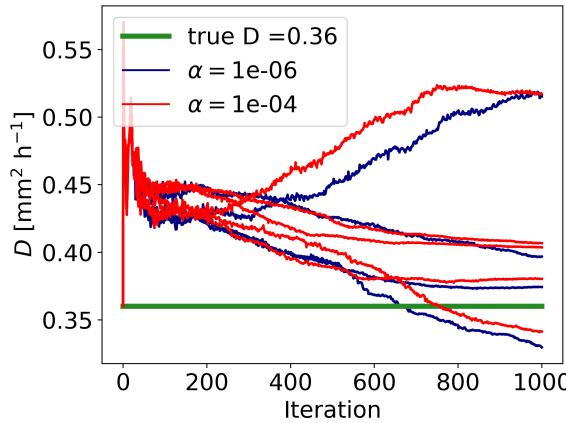


Fig. 14: Convergence plots for the FEM regularization parameters presented in table III.

C. Residual based refinement

Algorithm 2 Refinement step with the RAR algorithm as in "Procedure 2.2" in [34] adapted to the nomenclature in our work.

Input: The set of N PDE points \mathcal{P} , PDE residual $r(x, t)$, number m of points to add per refinement step, number n of points to test the residual

Output: refined PDE points \mathcal{P}

- 1: Compute the absolute value of the PDE residual $|r(x, t)|$ at n random samples $\mathcal{S} = \{(x_1, t_1), \dots, (x_n, t_n)\}$ from $\Omega_P \times [0, T]$
- 2: Sort \mathcal{S} by decreasing residual $|r(x, t)|$ and keep only the first m points
- 3: **return** The set of $N + m$ refined points $\mathcal{P} \cup \mathcal{S}$

Algorithm 3 Refinement step with the RAE algorithm, a modification of the RAR algorithm as described under "Procedure 2.2" in [34].

Input: The set of N PDE points \mathcal{P} , PDE residual $r(x, t)$, number m of points to add per refinement step, number n of points to test the residual

Output: refined PDE points \mathcal{P}

- 1: Compute the absolute value of the PDE residual $|r(x, t)|$ at n random samples $\mathcal{S} = \{(x_1, t_1), \dots, (x_n, t_n)\}$ from $\Omega_P \times [0, T]$
- 2: Sort \mathcal{S} by decreasing residual $|r(x, t)|$ and keep only the first m points
- 3: Compute the PDE residual $|r_{\mathcal{P}}(x, t)|$ at the points in \mathcal{P}
- 4: Sort \mathcal{P} by increasing residual $|r_{\mathcal{P}}(x, t)|$ and keep only the first $n - m$ points
- 5: **return** The set of N refined points $\mathcal{P} \cup \mathcal{S}$

ACKNOWLEDGMENT

We would like to thank Lars Magnus Valnes for insightful discussions and providing scripts for preprocessing the MRI data and meshing. We would like to thank George Karniadakis,

Xuhui Meng, Khemraj Shukla and Shengze Cai from Brown University for helpful discussions about PINNs in the early stages of this work. We note and thankfully acknowledge G. Karniadakis' suggestion to switch to ℓ^1 loss during the optimization. The optimal control computations were performed on resources provided by Sigma2 - the National Infrastructure for High Performance Computing and Data Storage in Norway. The PINN results presented in this paper have been computed on the Experimental Infrastructure for Exploration of Exascale Computing (eX3), which is financially supported by the Research Council of Norway under contract 270053.

REFERENCES

- [1] G. E. Karniadakis, I. G. Kevrekidis, L. Lu, P. Perdikaris, S. Wang, and L. Yang, "Physics-informed machine learning," *Nature Reviews Physics*, May 2021. [Online]. Available: <http://www.nature.com/articles/s42254-021-00314-5>
- [2] M. Raissi, P. Perdikaris, and G. Karniadakis, "Physics-informed neural networks: A deep learning framework for solving forward and inverse problems involving nonlinear partial differential equations," *Journal of Computational Physics*, vol. 378, pp. 686–707, Feb. 2019. [Online]. Available: <https://linkinghub.elsevier.com/retrieve/pii/S0021999118307125>
- [3] S. Cuomo, V. S. di Cola, F. Giampaolo, G. Rozza, M. Raissi, and F. Piccialli, "Scientific Machine Learning through Physics-Informed Neural Networks: Where we are and What's next," *arXiv:2201.05624 [physics]*, Jan. 2022, arXiv: 2201.05624. [Online]. Available: <http://arxiv.org/abs/2201.05624>
- [4] S. H. Rudy, S. L. Brunton, J. L. Proctor, and J. N. Kutz, "Data-driven discovery of partial differential equations," *Science Advances*, vol. 3, no. 4, p. e1602614, Apr. 2017. [Online]. Available: <https://advances.sciencemag.org/lookup/doi/10.1126/sciadv.1602614>
- [5] G. C. Y. Peng, M. Alber, A. Buganza Tepole, W. R. Cannon, S. De, S. Dura-Bernal, K. Garikipati, G. Karniadakis, W. W. Lytton, P. Perdikaris, L. Petzold, and E. Kuhl, "Multiscale Modeling Meets Machine Learning: What Can We Learn?" *Archives of Computational Methods in Engineering*, vol. 28, no. 3, pp. 1017–1037, May 2021. [Online]. Available: <https://doi.org/10.1007/s11831-020-09405-5>
- [6] N. Rahaman, A. Baratin, D. Arpit, F. Draxler, M. Lin, F. Hamprecht, Y. Bengio, and A. Courville, "On the Spectral Bias of Neural Networks," in *Proceedings of the 36th International Conference on Machine Learning*. PMLR, May 2019, pp. 5301–5310, iSSN: 2640-3498. [Online]. Available: <https://proceedings.mlr.press/v97/rahaman19a.html>
- [7] X. Jin, S. Cai, H. Li, and G. E. Karniadakis, "NSFnets (Navier-Stokes flow nets): Physics-informed neural networks for the incompressible Navier-Stokes equations," *Journal of Computational Physics*, vol. 426, p. 109951, Feb. 2021. [Online]. Available: <https://www.sciencedirect.com/science/article/pii/S0021999120307257>
- [8] B. Reyes, A. A. Howard, P. Perdikaris, and A. M. Tartakovsky, "Learning Unknown Physics of non-Newtonian Fluids," *arXiv:2009.01658 [physics]*, Aug. 2020, arXiv: 2009.01658. [Online]. Available: <http://arxiv.org/abs/2009.01658>
- [9] A. Arzani, J.-X. Wang, and R. M. D'Souza, "Uncovering near-wall blood flow from sparse data with physics-informed neural networks," *Physics of Fluids*, vol. 33, no. 7, p. 071905, Jul. 2021, publisher: American Institute of Physics. [Online]. Available: <https://aip.scitation.org/doi/10.1063/5.0055600>
- [10] S. Cai, Z. Wang, F. Fuest, Y. J. Jeon, C. Gray, and G. E. Karniadakis, "Flow over an espresso cup: inferring 3-D velocity and pressure fields from tomographic background oriented Schlieren via physics-informed neural networks," *Journal of Fluid Mechanics*, vol. 915, p. A102, May 2021. [Online]. Available: https://www.cambridge.org/core/product/identifier/S002211202100135X/type/journal_article
- [11] G. Kissas, Y. Yang, E. Hwuang, W. R. Witschey, J. A. Detre, and P. Perdikaris, "Machine learning in cardiovascular flows modeling: Predicting arterial blood pressure from non-invasive 4D flow MRI data using physics-informed neural networks," *Computer Methods in Applied Mechanics and Engineering*, vol. 358, p. 112623, Jan. 2020. [Online]. Available: <http://www.sciencedirect.com/science/article/pii/S0045782519305055>

[12] S. Cai, Z. Mao, Z. Wang, M. Yin, and G. E. Karniadakis, "Physics-informed neural networks (PINNs) for fluid mechanics: A review," *arXiv:2105.09506 [physics]*, May 2021, arXiv: 2105.09506. [Online]. Available: <http://arxiv.org/abs/2105.09506>

[13] J. J. Iliff, M. Wang, Y. Liao, B. A. Plogg, W. Peng, G. A. Gundersen, H. Benveniste, G. E. Vates, R. Deane, S. A. Goldman, E. A. Nagelhus, and M. Nedergaard, "A Paravascular Pathway Facilitates CSF Flow Through the Brain Parenchyma and the Clearance of Interstitial Solutes, Including Amyloid beta," *Science Translational Medicine*, vol. 4, no. 147, pp. 147ra111–147ra111, Aug. 2012, publisher: American Association for the Advancement of Science Section: Research Article. [Online]. Available: <https://stm.sciencemag.org/content/4/147/147ra111>

[14] M. Nedergaard and S. A. Goldman, "Glymphatic failure as a final common pathway to dementia," *Science (New York, N.Y.)*, vol. 370, no. 6512, pp. 50–56, Oct. 2020. [Online]. Available: <https://www.ncbi.nlm.nih.gov/pmc/articles/PMC8186542/>

[15] H. Mestre, J. Tithof, T. Du, W. Song, W. Peng, A. M. Sweeney, G. Olveda, J. H. Thomas, M. Nedergaard, and D. H. Kelley, "Flow of cerebrospinal fluid is driven by arterial pulsations and is reduced in hypertension," *Nature Communications*, vol. 9, no. 1, p. 4878, Dec. 2018. [Online]. Available: <http://www.nature.com/articles/s41467-018-07318-3>

[16] G. Ringstad, L. M. Valnes, A. M. Dale, A. H. Pripp, S.-A. S. Vatnehol, K. E. Emblem, K.-A. Mardal, and P. K. Eide, "Brain-wide glymphatic enhancement and clearance in humans assessed with MRI," *JCI Insight*, vol. 3, no. 13, p. e121537, Jul. 2018. [Online]. Available: <https://insight.jci.org/articles/view/121537>

[17] K. E. Holter, B. Kehlet, A. Devor, T. J. Sejnowski, A. M. Dale, S. W. Omholt, O. P. Ottersen, E. A. Nagelhus, K.-A. Mardal, and K. H. Pettersen, "Interstitial solute transport in 3D reconstructed neuropil occurs by diffusion rather than bulk flow," *Proceedings of the National Academy of Sciences*, vol. 114, no. 37, pp. 9894–9899, Sep. 2017, publisher: National Academy of Sciences Section: Biological Sciences. [Online]. Available: <https://www.pnas.org/content/114/37/9894>

[18] S. B. Hladky and M. A. Barrand, "The glymphatic hypothesis: the theory and the evidence," *Fluids and Barriers of the CNS*, vol. 19, no. 1, p. 9, Feb. 2022. [Online]. Available: <https://doi.org/10.1186/s12987-021-00282-z>

[19] R. T. Kedarasetti, P. J. Drew, and F. Costanzo, "Arterial pulsations drive oscillatory flow of CSF but not directional pumping," *Scientific Reports*, vol. 10, no. 1, p. 10102, Jun. 2020, number: 1 Publisher: Nature Publishing Group. [Online]. Available: <https://www.nature.com/articles/s41598-020-66887-w>

[20] A. Ladrón-de Guevara, J. K. Shang, M. Nedergaard, and D. H. Kelley, "Perivascular pumping in the mouse brain: Improved boundary conditions reconcile theory, simulation, and experiment," *Journal of Theoretical Biology*, p. 111103, 2022.

[21] A. J. Smith and A. S. Verkman, "Going against the flow: Interstitial solute transport in brain is diffusive and aquaporin-4 independent," *The Journal of physiology*, vol. 597, no. 17, pp. 4421–4424, Sep. 2019. [Online]. Available: <https://www.ncbi.nlm.nih.gov/pmc/articles/PMC6717017/>

[22] L. Ray, J. J. Iliff, and J. J. Heys, "Analysis of convective and diffusive transport in the brain interstitium," *Fluids and Barriers of the CNS*, vol. 16, no. 1, p. 6, Dec. 2019. [Online]. Available: <https://fluidsbarrierscns.biomedcentral.com/articles/10.1186/s12987-019-0126-9>

[23] L. A. Ray, M. Pike, M. Simon, J. J. Iliff, and J. J. Heys, "Quantitative analysis of macroscopic solute transport in the murine brain," *Fluids and Barriers of the CNS*, vol. 18, no. 1, p. 55, Dec. 2021. [Online]. Available: <https://doi.org/10.1186/s12987-021-00290-z>

[24] L. M. Valnes, S. K. Mitusch, G. Ringstad, P. K. Eide, S. W. Funke, and K.-A. Mardal, "Apparent diffusion coefficient estimates based on 24 hours tracer movement support glymphatic transport in human cerebral cortex," *Scientific Reports*, vol. 10, no. 1, p. 9176, Jun. 2020, number: 1 Publisher: Nature Publishing Group. [Online]. Available: <https://www.nature.com/articles/s41598-020-66042-5>

[25] A. L. Alexander, J. E. Lee, M. Lazar, and A. S. Field, "Diffusion Tensor Imaging of the Brain," *Neurotherapeutics*, vol. 4, no. 3, pp. 316–329, Jul. 2007. [Online]. Available: <https://www.sciencedirect.com/science/article/pii/S1933721307000955>

[26] S. Cai, Z. Wang, C. Chrysostomidis, and G. E. Karniadakis, "Heat Transfer Prediction With Unknown Thermal Boundary Conditions Using Physics-Informed Neural Networks," in *Volume 3: Computational Fluid Dynamics; Micro and Nano Fluid Dynamics*. Virtual, Online: American Society of Mechanical Engineers, Jul. 2020, p. V003T05A054. [Online]. Available: <https://asmedigitalcollection.asme.org/FEDSM/proceedings/FEDSM2020/83730/Virtual,%20Online/1088155>

[27] E. Syková and C. Nicholson, "Diffusion in Brain Extracellular Space," *Physiological Reviews*, vol. 88, no. 4, pp. 1277–1340, Oct. 2008. [Online]. Available: <https://www.physiology.org/doi/10.1152/physrev.00027.2007>

[28] B. Fischl, "FreeSurfer," *NeuroImage*, vol. 62, no. 2, pp. 774–781, Aug. 2012. [Online]. Available: <https://www.sciencedirect.com/science/article/pii/S1053811912000389>

[29] K. Ito and K. Kunisch, "On the Choice of the Regularization Parameter in Nonlinear Inverse Problems," *SIAM Journal on Optimization*, vol. 2, no. 3, pp. 376–404, Aug. 1992. [Online]. Available: <http://pubs.siam.org/doi/10.1137/0802019>

[30] G. Holler, K. Kunisch, and R. C. Barnard, "A bilevel approach for parameter learning in inverse problems," *Inverse Problems*, vol. 34, no. 11, p. 115012, Nov. 2018. [Online]. Available: <https://iopscience.iop.org/article/10.1088/1361-6420/aae77>

[31] B. Kaltenbacher, A. Kirchner, and B. Vexler, "Adaptive discretizations for the choice of a Tikhonov regularization parameter in nonlinear inverse problems," *Inverse Problems*, vol. 27, no. 12, p. 125008, Dec. 2011. [Online]. Available: <https://iopscience.iop.org/article/10.1088/0266-5611/27/12/125008>

[32] M. Hinze, R. Pinnau, M. Ulbrich, and S. Ulbrich, *Optimization with PDE constraints*. Springer Science & Business Media, 2008, vol. 23.

[33] X. Glorot and Y. Bengio, "Understanding the difficulty of training deep feedforward neural networks," in *Proceedings of the Thirteenth International Conference on Artificial Intelligence and Statistics*. JMLR Workshop and Conference Proceedings, Mar. 2010, pp. 249–256, iSSN: 1938-7228. [Online]. Available: <https://proceedings.mlr.press/v9/glorot10a.html>

[34] L. Lu, X. Meng, Z. Mao, and G. E. Karniadakis, "DeepXDE: A Deep Learning Library for Solving Differential Equations," *SIAM Review*, vol. 63, no. 1, pp. 208–228, Jan. 2021, publisher: Society for Industrial and Applied Mathematics. [Online]. Available: <https://epubs.siam.org/doi/abs/10.1137/19M1274067>

[35] D. P. Kingma and J. Ba, "Adam: A Method for Stochastic Optimization," *arXiv:1412.6980 [cs]*, Jan. 2017, arXiv: 1412.6980. [Online]. Available: <http://arxiv.org/abs/1412.6980>

[36] I. Goodfellow, Y. Bengio, and A. Courville, *Deep Learning*. MIT Press, 2016, <http://www.deeplearningbook.org>.

[37] M. S. Aln, B. Kehlet, A. Logg, C. Richardson, J. Ring, E. Rognes, and G. N. Wells, "The FEniCS Project Version 1.5," p. 15, 2015.

[38] S. K. Mitusch, S. W. Funke, and J. S. Dokken, "dolfin-adjoint 2018.1: automated adjoints for FEniCS and Firedrake," *Journal of Open Source Software*, vol. 4, no. 38, p. 1292, Jun. 2019. [Online]. Available: <https://joss.theoj.org/papers/10.21105/joss.01292>

[39] M. Croci, V. Vinje, and M. E. Rognes, "Uncertainty quantification of parenchymal tracer distribution using random diffusion and convective velocity fields," *Fluids and Barriers of the CNS*, vol. 16, no. 1, p. 32, Dec. 2019. [Online]. Available: <https://fluidsbarrierscns.biomedcentral.com/articles/10.1186/s12987-019-0152-7>

[40] S. Koundal, R. Elkin, S. Nadeem, Y. Xue, S. Constantinou, S. Sanggaard, X. Liu, B. Monte, F. Xu, W. Van Nostrand, M. Nedergaard, H. Lee, J. Wardlaw, H. Benveniste, and A. Tannenbaum, "Optimal Mass Transport with Lagrangian Workflow Reveals Advection and Diffusion Driven Solute Transport in the Glymphatic System," *Scientific Reports*, vol. 10, no. 1, p. 1990, Dec. 2020. [Online]. Available: <https://www.nature.com/articles/s41598-020-59045-9>

[41] SVMTK, "SurfaceVolumeMeshingToolKit," Nov. 2021, original date: 2017-09-22T15:36:28Z. [Online]. Available: <https://github.com/SVMTK/SVMTK>

[42] T. C. Project, *{CGAL} User and Reference Manual*, 5th ed. CGAL Editorial Board, 2022. [Online]. Available: <https://doc.cgal.org/5.4/Manual/packages.html>

[43] K.-A. Mardal, M. E. Rognes, T. B. Thompson, and L. M. Valnes, "Simulating Anisotropic Diffusion in Heterogeneous Brain Regions," in *Mathematical Modeling of the Human Brain: From Magnetic Resonance Images to Finite Element Simulation*, ser. Simula SpringerBriefs on Computing, K.-A. Mardal, M. E. Rognes, T. B. Thompson, and L. M. Valnes, Eds. Cham: Springer International Publishing, 2022, pp. 97–107. [Online]. Available: https://doi.org/10.1007/978-3-030-95136-8_6

[44] T. Kadeethum, T. M. Jørgensen, and H. M. Nick, "Physics-informed Neural Networks for Solving Inverse Problems of Nonlinear Biot's Equations: Batch Training," *arXiv:2005.09638 [physics]*, May 2020, arXiv: 2005.09638. [Online]. Available: <http://arxiv.org/abs/2005.09638>

[45] A. Mathews, M. Francisquez, J. W. Hughes, D. R. Hatch, B. Zhu, and B. N. Rogers, "Uncovering turbulent plasma dynamics

via deep learning from partial observations,” *Physical Review E*, vol. 104, no. 2, p. 025205, Aug. 2021. [Online]. Available: <https://link.aps.org/doi/10.1103/PhysRevE.104.025205>

[46] S. Wang, X. Yu, and P. Perdikaris, “When and why PINNs fail to train: A neural tangent kernel perspective,” *Journal of Computational Physics*, vol. 449, p. 110768, Jan. 2022. [Online]. Available: <https://www.sciencedirect.com/science/article/pii/S002199912100663X>

[47] S. Wang, H. Wang, and P. Perdikaris, “On the eigenvector bias of Fourier feature networks: From regression to solving multi-scale PDEs with physics-informed neural networks,” *arXiv:2012.10047 [cs, stat]*, Dec. 2020, arXiv: 2012.10047. [Online]. Available: <http://arxiv.org/abs/2012.10047>

[48] R. van der Meer, C. Oosterlee, and A. Borovykh, “Optimally weighted loss functions for solving PDEs with Neural Networks,” *arXiv:2002.06269 [cs, math]*, Mar. 2021, arXiv: 2002.06269. [Online]. Available: <http://arxiv.org/abs/2002.06269>

[49] B. Kaltenbacher, A. Neubauer, and O. Scherzer, *Iterative Regularization Methods for Nonlinear Ill-Posed Problems*. De Gruyter, Sep. 2008, publication Title: Iterative Regularization Methods for Nonlinear Ill-Posed Problems. [Online]. Available: <https://www.degruyter.com/document/doi/10.1515/9783110208276/html>